



# Axially coordinated dual-atomic-site catalysts for nearly 100% peroxyomonosulfate conversion to ${}^1\text{O}_2$ in membrane filtration

Hanwen Gong <sup>a</sup>, Lingling Xu <sup>a</sup>, Cong Li <sup>a</sup>, Meilan Pan <sup>a,\*</sup>, Minghua Zhou <sup>b,\*</sup>

<sup>a</sup> College of Environment, Zhejiang University of Technology, Hangzhou, Zhejiang 310014, China

<sup>b</sup> Key Laboratory of Pollution Process and Environmental Criteria, Ministry of Education, Carbon Neutrality Interdisciplinary Science Centre, College of Environmental Science and Engineering, Nankai University, Tianjin 300350, China



## ARTICLE INFO

### Keywords:

Dual-atomic-site catalysts  
Axial coordination  
Singlet oxygen  
Co-Mn sites  
Environmental remediation

## ABSTRACT

Reactive membrane filtration, integrating membrane technology with catalytic processes, offers a promising avenue for efficiently generating and utilizing active species in environmental remediation. Herein, a dual-atom Co-Mn site achieved through axial coordination on N-doped graphene catalyst (*sp*-CoMn@NG) has been developed and applied in membrane filtration for the targeted removal of specific pollutants. Experimental investigations, alongside density functional theory (DFT) calculations, have substantiated that axial coordination can effectively reduce the adsorption energy and activation barrier of PMS, thereby facilitating nearly 100% conversion of PMS to  ${}^1\text{O}_2$  and enhancing catalytic performance. Mechanistic studies further elucidate the  ${}^1\text{O}_2$  production mechanism through a superoxide-mediated chain reaction at the axially coordinated Co-Mn center, as well as the inactivation mechanism of catalytic membranes via the addition reaction of  ${}^1\text{O}_2$  and phenolic-hydroxyl compounds. This research underscores the intelligent prefabrication of axial coordination in dual-atomic-site catalysts, offering an efficient approach for scalable  ${}^1\text{O}_2$  production in reactive membrane filtration.

## 1. Introduction

The presence of various organic pollutants in the aquatic environment poses significant threats to human health and the survival of various organisms, resulting in severe harm to the ecological balance [1, 2]. To date, several technologies have been employed to address such pollutants, encompassing adsorption, membrane separation, and the advanced oxidation process (AOPs) [3,4]. Particularly, persulfate-based AOPs (PS-AOPs) have emerged as a promising approach for degrading aqueous organic pollutants due to their ability to generate reactive oxygen species (ROS), including sulphate radical ( $\text{SO}_4^{\cdot-}$ ), hydroxyl radical ( ${}^{\cdot}\text{OH}$ ), and singlet oxygen ( ${}^1\text{O}_2$ ) [5,6]. Notably,  ${}^1\text{O}_2$  denotes an excited state of  $\text{O}_2$  featuring an unoccupied  $\pi^*$  orbital, recognizing as a potent oxidant with a lengthy half-life of  $10^{-5}$  s, displaying superior resistance to environmental interference and enhanced selectivity for degradation compared to  $\text{SO}_4^{\cdot-}$  and  ${}^{\cdot}\text{OH}$  [7–9]. Nonetheless, the production of  ${}^1\text{O}_2$  via PS activation invariably accompanies the generation of other ROS. Therefore, the pursuit of novel approaches for highly selective  ${}^1\text{O}_2$  production holds paramount importance, not only for investigating  ${}^1\text{O}_2$ -associated degradation processes but also for advancing material development.

Atomic-site catalysts (ASCs) with high catalytic efficiency have been utilized to activate PMS, generating  ${}^1\text{O}_2$  for the degradation of persistent pollutants [10–12]. N-doped carbon supported ASCs, featuring the distinctive structure of M-N-C, have demonstrated significantly enhanced selective  ${}^1\text{O}_2$  generation through PMS activation [13–15]. In pursuit of ASCs with exceptional performance and appreciable selectivity, extensive research has been focused on adjusting coordination configurations and electronic properties [16]. Particularly, coordination engineering emerges as an efficient approach for enhancing catalytic performance by manipulating direct coordination atoms or environmental atoms [17]. Unlike classical planar coordination engineering, axial coordination modification can impart ASCs with novel electronic and chemical properties, leading to significant enhancements in electrocatalytic performance [18]. On the other hand, dual-atomic-site catalysts (DASCs) employ two adjacent atomic metal species for their complementary functionalities and synergistic actions [19], offering new avenues for modulating electric and geometric structure with inherently enhanced performance. Consequently, the coordination regulation of DASCs is crucial for the selectively producing  ${}^1\text{O}_2$  through PMS activation, albeit it remains highly challenging.

Reactive membrane filtration, which integrates membrane

\* Corresponding authors.

E-mail addresses: [mlpan@zjut.edu.cn](mailto:mlpan@zjut.edu.cn) (M. Pan), [zhoumh@nankai.edu.cn](mailto:zhoumh@nankai.edu.cn) (M. Zhou).

technology with catalytic processes, offers advantages such as enhanced mass and charge transfer, rendering it a promising approach for utilizing  $^1\text{O}_2$  in environmental cleanup efforts [20,21]. Within the context of reactive membrane filtration,  $^1\text{O}_2$  can be generated *in-situ* within or in close proximity to the membrane material, enabling direct contact with target pollutants as they pass through the membrane pores. This setup enhances contaminant removal efficiency by promoting rapid and localized oxidation reactions at the membrane surface or within its matrix [22–24]. Moreover, the utilization of membranes in tandem with  $^1\text{O}_2$  provides additional benefits, including improved mass transfer, heightened selectivity, and reduced fouling compared to conventional treatment strategies [25–27]. Membranes serve as physical barriers that selectively separates pollutants based on size, charge, or chemical affinity, while also facilitating the transport of PMS to active sites [28]. Nonetheless, the durability of catalytic membranes poses a significant challenge, as it can be easily compromised by the accumulation of large amounts of intermediates, leading to active site poisoning during PS-AOPs processes.

Herein, we developed an axially coordinated dual-atom Co-Mn site on an N-doped graphene catalyst (*sp*-CoMn@NG), achieving almost 100% conversion of PMS to  $^1\text{O}_2$  in a flow-through membrane system. Such  $^1\text{O}_2$ -mediated membrane catalysis on DASCs enabled effective *in-situ* degradation of organic pollutants, exhibiting a significantly higher rate constant for levofloxacin degradation, approximately 150 times that of NG alone. We confirmed the presence of  $^1\text{O}_2$  and investigated its evolution pathway triggered by dissolved oxygen (DO) during the PMS activation process. Experimental and density functional theory (DFT) calculations elucidated the individual roles of Co and Mn atoms on *sp*-CoMn@NG, as well as the relationship between axial coordination structure and selective degradation. Subsequently, we assessed the durable degradation of organic compounds with varying electron donating/withdrawing abilities of functional groups, and proposed a mechanism of active site poisoning for phenolic organic compounds through a series of sequential  $^1\text{O}_2$ -mediated addition reactions.

## 2. Experimental section/methods

### 2.1. Chemicals

All chemicals were used as received without further purification, and the complete list with details is provided in SI Appendix. Ultrapure water with a resistivity of  $18.2\text{ M}\Omega\text{ cm}^{-1}$  (Smart-Q15, Hitech, China) was used for all experiments.

### 2.2. Synthesis of catalysts

Graphite oxide (GO) was synthesized using a modified Hummers' method [29], and N-doped graphene (NG) was synthesized as our previous reports [30], and it was applied as the precursor for single atom doped graphene materials. To synthesize axial coordinated Co and Mn dual doped graphene (*sp*-CoMn@NG), NG (1 mg  $\text{mL}^{-1}$ ) was dispersed in DMF solution, dopamine (2 mM), and mixed with  $\text{Co}^{2+}$  ( $\text{Co}(\text{NO}_3)_2 \cdot 6\text{ H}_2\text{O}$ , 1 mg  $\text{mL}^{-1}$ ) and  $\text{Mn}^{2+}$  ( $\text{MnCl}_4 \cdot 4\text{ H}_2\text{O}$ , 1 mg  $\text{mL}^{-1}$ ), and the mixture was ultrasonicated for 20 min until complete dissolution. The resultant solution was transferred to a three-necks flask and reacted at  $60^\circ\text{C}$  for 12 hours in an oil bath. Then, the suspension was centrifuged to remove the free  $\text{Co}^{2+}$  and  $\text{Mn}^{2+}$  in DMF, and the yield solid product was washed with ethanol and DI water. The obtained products were freeze-dried and then annealed under argon atmosphere at  $500^\circ\text{C}$  in the rate of  $2^\circ\text{C}/\text{min}$  for 3 h. Finally, to remove the residual Co and Mn oxides, the above materials were washed by 0.5 M HCl solution and then DI water to yield *sp*-CoMn@NG. For *p*-CoMn@NG, the protocol was the same, except the co-addition of dopamine. For Co@NG and Mn@NG, the protocol was the same, except the co-addition of  $\text{Co}^{2+}$  and  $\text{Mn}^{2+}$  was replaced by the only addition of  $\text{Co}^{2+}$  or  $\text{Mn}^{2+}$  in the first step, respectively.

### 2.3. Materials characterization

The X-ray absorption spectra (XAS) including X-ray absorption near-edge structure (XANES) and extended X-ray absorption fine structure (EXAFS) of the sample at Co and Mn K-edge was collected at the Beamline of TLS07A1 in National Synchrotron Radiation Research Center (NSRRC), Taiwan. HAADF-STEM and the corresponding EELS were conducted on a Titan Themis G2 60–300 scanning/transmission electron microscope. The microstructure and morphology of the material were characterized by Scanning electron microscope (SEM, Hitachi, Japan) and Transmission electron microscopy (TEM, FEI, USA). The materials were analyzed by Diffractometer (XRD, Empyrean, Netherlands). The surface functional groups of the material were characterized by X-ray photoelectron spectroscopy (XPS, Shimadzu, Japan). The molecular structure and chemical composition of the materials were analyzed by Raman spectroscopy (Renishaw, UK) and Fourier transform infrared spectroscopy (FT-IR, Bruker, Germany). The contaminants are cross-linked and polymerized on the catalyst surface to form polymeric substances. Low resolution mass spectrometry (LR-MS, AB SCIEX TripleQuad 3500, USA) was used to analyze the dissolved products after the polymerization was dissolved in acetonitrile. Electron paramagnetic resonance (EPR) verified the active species in the reaction. The current response and impedance testing of the material are used to detect the electrochemical workstation CHI 660E.

### 2.4. Experimental setup and methodology

This study used a flow filtration device to conduct material performance experiments. The 10 mg prepared sample was dispersed in DMF by ultrasonic crusher for 25 min (Beidi-900TE). Then, the sample was filtered using a 0.8  $\mu\text{m}$  microporous filter membrane. The sample was then rinsed with 100 mL ethanol and water to remove any residual DMF. Finally, the surface-coated membrane is loaded into the filter box. The peristaltic pump then delivers the LVF solution through the membrane at a flow rate of 0.5 mL/min. The sample is collected directly from the casing outlet with an automatic partial collector (BSZ-100) and analyzed immediately.

## 3. Results and discussion

### 3.1. Characterization of axially coordinated *sp*-CoMn@NG catalyst

Downsizing the catalysts to be atomic-site catalysts (ASCs) is an efficient way to improve the metal utilization (Fig. 1a). The regulation of coordination microenvironment (e.g., planar and stereo structure) has been regarded as an efficient strategy to optimize the electron structure of ASCs (Fig. 1b). For systematic study of coordination microenvironment effects on the property and catalytic activity of Co and Mn dual-atomic-site catalysts, Co-Mn dual active site with a planar structure (*p*-CoMn@NG) and Co-Mn dual site with an axial coordination structure (*s*-CoMn@NG) were synthesized. Fig. 1c shows the partial density of states (PDOS) of Co and Mn d band, suggesting that the upshift of d band center on *s*-CoMn@NG. According to the d band theory, the upshifts of d band center would result in a decrease in the electron filling in the anti-bonding states, thus facilitating the reaction intermediates to be adsorbed on *s*-CoMn@NG surface more easily [31]. Notably, N-doped graphene (NG) plays a crucial role in ASCs catalysts by providing active sites, enhancing electron transfer, stabilizing atomic metal, and facilitating synergistic effects to improve the efficiency and selectivity of catalytic reactions [32]. The synthesis process involved preparing NG as the support material, utilizing dopamine as an axial bridge for coordinating  $\text{Co}^{2+}$  and  $\text{Mn}^{2+}$ , conducting post-synthetic ion-exchange for uniform distribution of metal ions, and subjecting the mixture to high-temperature pyrolysis to construct axial coordination (Fig. 1d) [16]. During fabrication, Co and Mn sites were inevitably co-doped onto a planar structure, resulting in the coexistence of planar and axially

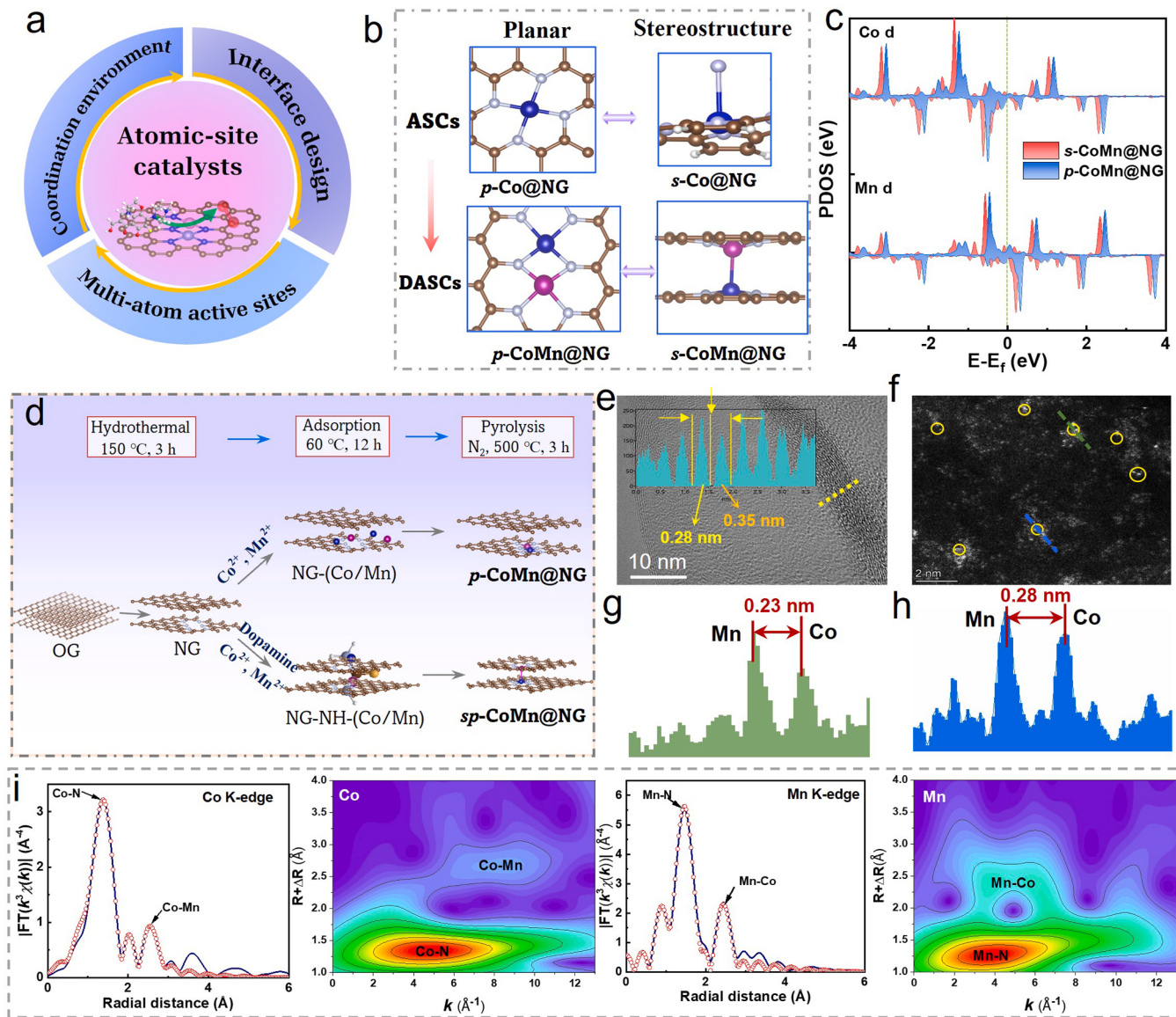


**Fig. 1.** (a) Motivation and design of atomic-site catalysts. (b) Schematic illustration of the structures of ASCs and DASCs with different coordination environment. (c) The spin-resolved PDOS of Co and Mn on *s*-CoMn@NG and *p*-CoMn@NG. (d) Schematic of the formation of dual metal Co-Mn sites on *s*-CoMn@NG and *sp*-CoMn@NG. HR-TEM (e) and aberration-corrected HAADF-STEM (f) images of *sp*-CoMn@NG, and corresponding lattice peaks (g, h). (i) Wavelet transforms for the  $k^3$ -weighted EXAFS signals of Co SAs and Mn SAs in *sp*-CoMn@NG, and corresponding Co K-edge EXAFS fitting with Co centered neighboring Co-N and Co-Mn, and Mn K-edge EXAFS fitting with Mn centered neighboring Mn-N and Mn-Co.

coordinated structures, thus yielding *sp*-CoMn@NG. It's noteworthy that the absence of dopamine hindered the formation of axially coordinated Co-Mn sites, yet a planar structured dual-sites can still form, leading to the production of *p*-CoMn@NG catalyst.

The morphology and structure of the resulting *sp*-CoMn@NG presented the typical scrolls and wrinkles of graphene (Figs. S1–2), and no nanoparticles of metallic Co/Mn or Co/Mn oxides were observed, indicating that both Co and Mn were not decomposed under the synthesis conditions. The (002) plane peak of *sp*-CoMn@NG in XRD pattern (Fig. S3) shifted to higher angle of 20 with the Co and Mn co-dopants, attributing to the decrease of interlayer spacing. This result was also proved on HR-TEM, which displays a few layers of stacked nanosheets with two interlayer spacings of 0.28 and 0.35 nm (Fig. 1e). Note that the distance of 0.35 nm can be recognized as the interlayer spacing of NG nanosheets [33]. To corroborate the formation of Co and Mn atoms, aberration-corrected high-angle annular dark-field scanning transmission electron microscope (HAADF-STEM) with subangstrom

resolution measurement and electron energy loss spectroscopy (EELS) were performed. The signals for Mn (664.0 eV) and Co (784.5 eV) atoms were detected simultaneously in Fig. S4, suggesting the coexistence of Co and Mn atoms. A number of well-dispersed bright dots marked with yellow cycles were corresponding to heavier Co and Mn atoms (Fig. 1f–h), in which the statistic distance between adjacent bright spots is  $\sim 0.23$  and  $0.28$  nm, assigning to the distance of Co and Mn site in a planar and stereo structure, respectively. Additionally, the combined energy-dispersive X-ray spectroscopy (STEM-EDS) elemental distributions of Co and Mn were shown in Fig. S2c–f, in which the neighboring Co and Mn atoms were also observed.

The accurate content of Co and Mn elements in *sp*-CoMn@NG was detected by inductively coupled plasma atomic emission spectrometry (ICP-AES, Table S1). The content of Co and Mn atoms in *sp*-CoMn@NG is 0.75 wt% and 0.70 wt%, while the Co element in Co@NG is 1.78 wt% and Mn element in Mn@NG is 2.14 wt%. The high resolution XPS N 1 s spectra (Fig. S5 and Table S2) of Co@NG, Mn@NG, *p*-CoMn@NG, and

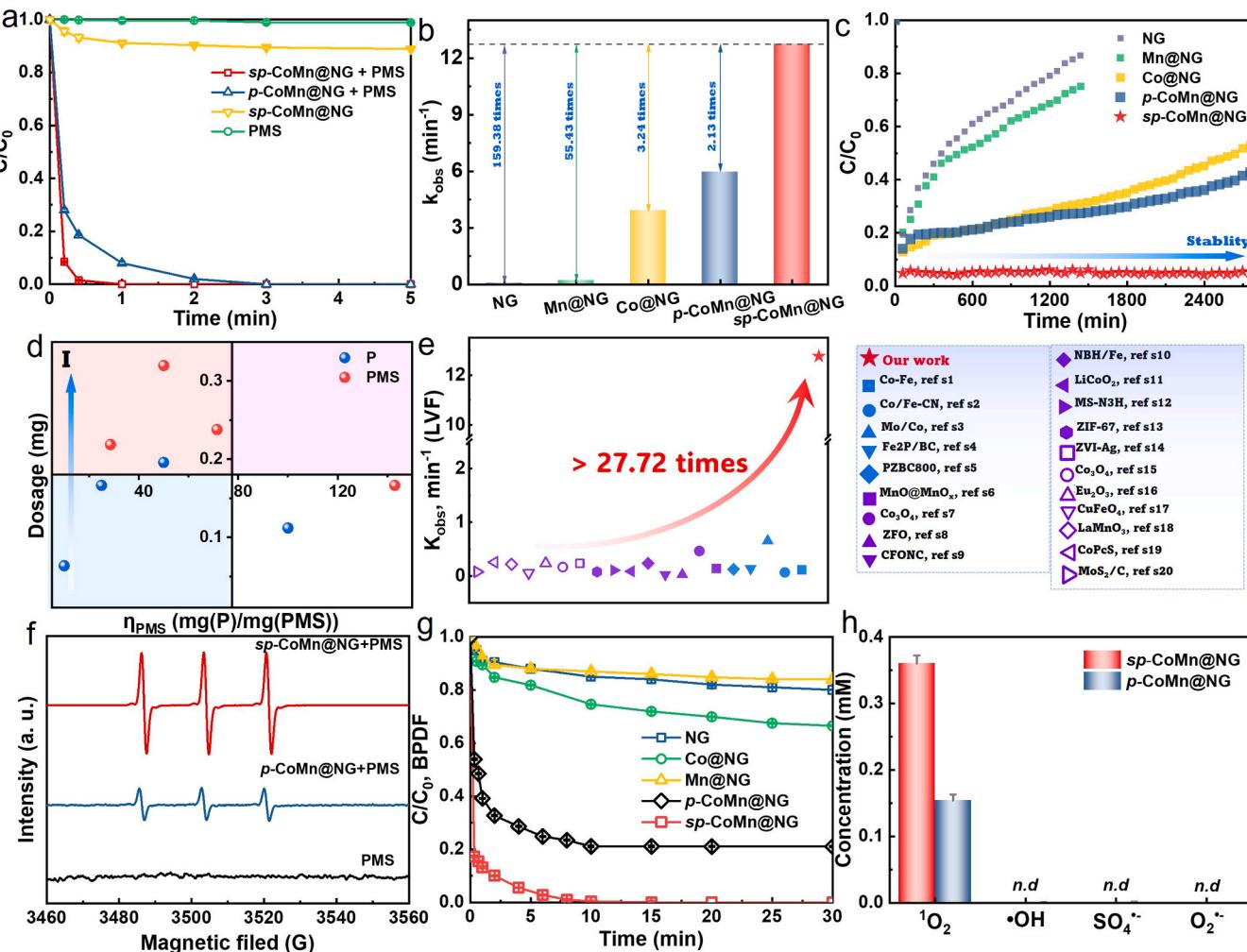


**Fig. 2.** (a) The removal of LVF on different conditions.  $[LVF] = 25 \pm 1 \text{ mg L}^{-1}$ ,  $[PMS] = 1.0 \pm 0.1 \text{ mM}$ ,  $pH = 5.8$ ,  $T = 25^\circ\text{C}$ ; (b) The rate constants of samples according to the degradation curves in the batching system (Fig. S12). (c) Stability of different samples in flowing-through system. (d) The relationship between PMS utilization efficiency and the dosage of PMS/degraded pollutants. (e) Comparison of *sp*-CoMn@NG and other reported advanced catalysts for LVF degradation by PMS activation. Note: s1-s20 is the corresponding references in supporting information (Table S4). (f) EPR spectra of *sp*-CoMn@NG system using TEMP as the spin-trapping agent. (g) The degradation of DPBF in *sp*-CoMn@NG/PMS, *p*-CoMn@NG/PMS, Co@NG/PMS, Mn@NG/PMS, and NG/PMS system. (h) The quantitative analyses of ROS in *sp*-CoMn@NG/PMS and *p*-CoMn@NG/PMS system. Note: *n.d* represents that none of radicals has been detected.

*sp*-CoMn@NG are assigned to five peaks, in which the peaks at 398.4, 399.0 eV, 399.8, 400.6 and 404.3 eV are corresponding to pyridinic N, metal (Co/Mn) N, pyrrolic N, graphitic N, and oxidized N, respectively. With the incorporation of metal atom, the content of pyridinic N increased, indicating the dominant coordination type of metal on N-species, which has been proved to be the possible Co-N<sub>4</sub> and Mn-N<sub>4</sub> structures [34]. In the Co 2p spectra, the peaks at 780.3 and 784.9 eV are Co 2p<sub>3/2</sub> (Co<sup>2+</sup>) orbits and corresponding satellite peak. The dominant peak of Mn 2p at 653.5 eV is assigned to Mn 2p<sub>3/2</sub> (Mn<sup>3+</sup>) orbits. Additionally, the Raman spectroscopy results (Fig. S6) revealed that the ratio of the D band to the G band intensity ( $I_D/I_G$ ) of *sp*-CoMn@NG (1.32) surpassed than that of Co@NG (1.31), Mn@NG (1.30), and NG (1.28), implying a more disordered carbon structure in *sp*-CoMn@NG. This higher ratio could be attributed to structural defects or disorder in the graphene lattice resulting from the incorporation of Co and Mn atoms. Moreover, the specific surface area and pore distribution of *sp*-CoMn@NG closely resembled those of *p*-CoMn@NG (Fig. S7), suggesting that the physical structure remained stable following the introduction of axial coordination.

To further reveal the structure of neighboring active centers in *sp*-CoMn@NG, synchrotron XAS analysis was performed. The normalized X-ray absorption near edge structure (XANES) curves of Co K-edge and

Mn K-edge in *sp*-CoMn@NG along with Co foil, CoO, Co<sub>3</sub>O<sub>4</sub>, Mn foil, MnO, and Mn<sub>2</sub>O<sub>3</sub> references were shown in Fig. S8. The near-edge absorption energy position of Co K-edge XANES spectra of *sp*-CoMn@NG is located between Co foil and CoO, demonstrating a valence state of Co between 0 and +2. While the Mn K-edge XANES spectra is situated between MnO and Mn<sub>2</sub>O<sub>3</sub>, suggesting a valence state of Mn at +2 ~ +3. The pre-edge peaks at 7709.3 and 6542.1 eV are ascribed to the 1s-4p transitions, suggesting the fingerprints of Co-N<sub>4</sub> and Mn-N<sub>4</sub> coordination [35]. Moreover, the  $k^3$ -weighted Fourier transforms (FT) of the extended X-ray absorption fine structure (EXAFS) at the Co K-edge demonstrates that the *sp*-CoMn@NG displays an obvious peak at 1.4 Å attributed to Co-N scattering, while the Co foil shows the Co-Co peaks at 2.2 Å and 4.0 Å, corresponding to the first and second coordinated shells of Co-Co scattering paths. Similarly, the FT-EXAFS at Mn K-edges presents a Mn-N peak at 1.5 Å. The metallic Co-Co and Mn-Mn peaks are negligible, which suggests that the Co and Mn atoms are atomically dispersed in *sp*-CoMn@NG. In addition, the wavelet transforms of K-edge EXAFS in Co foil, Mn foil and *sp*-CoMn@NG were shown in Fig. 1i. The wavelet transform contour plots of Co foil shows an intensity at 0.40 Å<sup>-1</sup> ( $R = 2.5$  Å, Table S3) corresponding to the shell of Co-Co coordination, while the *sp*-CoMn@NG displays intensity maximum at 0.53 Å<sup>-1</sup> ( $R = 1.9$  Å) reflecting the Co-N coordination. The Co and Mn configurations in

*sp*-CoMn@NG were fitted (Fig. S9–10), and both the  $k^3$ -weighted FT-EXAFS at Co and Mn K-edges are well-fitted by the inserting models of neighboring Co-N and Mn-N structure. The coordination numbers of Co and Mn centers are  $\sim 4.1 \pm 0.3$  and  $\sim 3.6 \pm 0.5$ , respectively, verifying the structure of Co-N<sub>4</sub> and Mn-N<sub>4</sub> active centers. Notably, the extra intensity at  $0.36 \text{ \AA}^{-1}$  ( $R = 2.8 \text{ \AA}$ ) could be ascribed to the Co-Mn coordination, indicating the existence of axial bond between neighboring Co-N<sub>4</sub> and Mn-N<sub>4</sub> centers. This result was further confirmed by the obvious intensity at  $0.36 \text{ \AA}^{-1}$  ( $R = 2.8 \text{ \AA}$ ) in Mn wavelet transform. Consequently, we proposed the spatial structure of *sp*-CoMn@NG, depicting an axially coordinated Co-Mn bond of approximately 0.28 nm and a planar Co-Mn bond of around 0.23 nm (Fig. S11), a configuration also supported by other literature reports [36].

### 3.2. Performance evaluation for PMS activation

The difference in the catalytic performance of *sp*-CoMn@NG activated PMS system was evaluated with levofloxacin (LVF, a representative refractory organic contaminant). It can be observed in Fig. 2a that the efficiency of *sp*-CoMn@NG activating PMS was significantly improved compared with that of *p*-CoMn@NG. *sp*-CoMn@NG was less effective (ca. 10%) in removing LVF without the addition of PMS, eliminating the effect of adsorption. Correspondingly, the catalytic rate constant ( $k_{\text{obs}}$ , Fig. 2b and S12) of *sp*-CoMn@NG increased by 2.1, 3.2, 55.4, and 159.4 times compared with that of *p*-CoMn@NG, Co@NG, Mn@NG, and NG, respectively. Note that the  $k_{\text{obs}}$  of LVF outperforms most catalysts in reported works, including ASCs, metal or metal oxides (Me), and non-metallic materials (NMe) (Fig. 2e and Table S4). The effects of various ubiquitous substances (Fig. S13), including anions (e.g., Cl<sup>-</sup>, HCO<sub>3</sub><sup>-</sup>, and SO<sub>4</sub><sup>2-</sup>) and cations (e.g., Na<sup>+</sup>, K<sup>+</sup>, Mg<sup>2+</sup>, and Ca<sup>2+</sup>), on the degradation efficiency were explored. The presence of anions resulted in a slight inhibition of 2,4-DCP removal, with the order of inhibition being HCO<sub>3</sub><sup>-</sup> > Cl<sup>-</sup> > SO<sub>4</sub><sup>2-</sup>. This inhibition is attributed to the consumption of ROS, an effect not observed in the presence of cations. Additionally, Fig. S14 demonstrated the remarkable removal efficiency of LVF (> 95%) using *sp*-CoMn@NG/PMS system for up to five consecutive reactions, with no significant changes or metal leaching observed in the repeated catalyst (Fig. S15).

Furthermore, *sp*-CoMn@NG could maintain complete degradation of 25 mg/L LVF at a flowrate of 0.5 mL/min more than 2700 min in the filtration membrane system (Fig. 2c), which is not the case of *p*-CoMn@NG, Co@NG, Mn@NG, and NG. As aforementioned, reactive membrane filtration serves for both physical separation by size and chemical reactions.[4] The exclusion of size effects was achieved through the utilization of membranes characterized by large pore sizes ( $\sim 0.8 \mu\text{m}$ ), surpassing the dimensions of the targeted pollutant molecules. Additionally, controlled operational parameters, including transmembrane pressure, crossflow velocity, and filtration duration, were carefully adjusted. Therefore, the observed enhancements in catalytic activity can plausibly be attributed to the synergistic effect between axial coordination microenvironment of *sp*-CoMn@NG and PMS activation. The PMS utilization efficiency ( $\eta_{\text{PMS}}$ , Fig. 2d and S16) of *sp*-CoMn@NG at various PMS/LVF concentrations was explored, offering valuable insights into optimizing the catalytic degradation process for efficient and sustainable wastewater treatment. Additionally, Fig. S17 illustrated a decrease in removal efficiency at a flowrate of 2 mL/min, attributed to the reduced retention time of active species on reactive sites within the catalyst. These results imply that *sp*-CoMn@NG can activate PMS rapidly and efficiently, achieving the durable performance for LVF degradation and giving a potential application in practical wastewater.

The EPR spectrum was used to further identify the ROS [37,38]. As shown in Fig. 2f, the strong triplet signals with an intensity ratio of 1:1:1 are observed in both *sp*-CoMn@NG/PMS/LVF/TEMP and *p*-CoMn@NG/PMS/LVF/TEMP system, implying the generation of  $^1\text{O}_2$ . Moreover, signals of DMPOX instead of DMPO-OH and DMPO-SO<sub>4</sub><sup>2-</sup> are

also observed, which formed from over-oxidation of DMPO by  $^1\text{O}_2$  or O<sub>2</sub><sup>•</sup> [10] (Fig. S18). Using 1,3-diphenylisobenzofuran (DPBF) as a probe, the possible generation of  $^1\text{O}_2$  was studied [39]. As shown in Fig. 2g, the *sp*-CoMn@NG/PMS system can rapidly degrade DPBF, which is much higher than *p*-CoMn@NG/PMS system, whereas other system (Co@NG/PMS, Mn@NG/PMS, and NG/PMS) is almost inactive, indicating that more  $^1\text{O}_2$  is generated in the former. Besides, the amount of generated ROS was further quantified employing p-benzoquinone (p-BQ), benzoic acid (BA), and nitrotetrazolium blue chloride (NBT) as probes for SO<sub>4</sub><sup>2-</sup>, OH, and O<sub>2</sub><sup>•</sup>, respectively. However, these radical species can not be detected, and only non-radical  $^1\text{O}_2$  with a concentration of 0.36 and 0.15 mM can be identified on *sp*-CoMn@NG and *p*-CoMn@NG, respectively (Fig. 2h). Based on the above results, it is reasonable to conclude that the construction of axial Co-Mn coordination enhanced the non-radical pathway with  $^1\text{O}_2$  for the activation of PMS.

### 3.3. Exploration of DO triggering axial coordinated sites for PMS activation

As aforementioned, axial coordinated sites largely improve the catalytic performance through  $^1\text{O}_2$ -mediated activation, so we further explore the origin of  $^1\text{O}_2$  production in the axial microenvironment (Fig. 3a). DO and PMS were previously reported as potential precursors for  $^1\text{O}_2$  generation. The degradation of LVF on *sp*-CoMn@NG was completely inhibited after introduction of N<sub>2</sub>, which is not the case of *p*-CoMn@NG, indicating DO was involved in the production of  $^1\text{O}_2$  in the *sp*-CoMn@NG/PMS system (Fig. S19). Furthermore, the TEMP- $^1\text{O}_2$  signals markedly disappeared (Fig. 3b), and the degradation of DPBF was significantly inhibited (Fig. 3c) upon the addition of N<sub>2</sub>. Conversely, the presence of O<sub>2</sub> slightly promoted the degradation efficiency of DPBF. These findings may be attributed to the contribution of O<sub>2</sub> to selective  $^1\text{O}_2$  production in the *sp*-CoMn@NG/PMS system, a pathway distinct from that observed in the *p*-CoMn@NG/PMS system.

To reveal the origin of the catalytic behaviors, the pathways of PMS activation were explored in a galvanic oxidation reactor, in which LVF can only be oxidized by the electron-transfer pathway. Fig. 3d showed a remarkable current increase on *sp*-CoMn@NG wrapped working electrode only when LVF, PMS and DO coexisted. This scenario indicated that the electron transfer from LVF to PMS and DO was occurred when the close interaction of both PMS/DO and LVF on the *sp*-CoMn@NG surface. Note that the significant characteristic peaks of O=S=O on both *sp*-CoMn@NG/PMS and *p*-CoMn@NG/PMS mixture presents a red-shift of 1061.0–1087.6 and 1137.8–1164.3 cm<sup>-1</sup>, respectively, verifying the electron transfer between PMS and Co-Mn sites (Fig. 3e). With the increased injection of PMS (Fig. 3f), a distinct positive current flow emerged promptly, witnessing the electron migration from *sp*-CoMn@NG wrapped electrode to PMS likely through the formation of surface-confined intermediates. Combined with the superior instinct electrical properties by the analysis of EIS (Fig. S20) and LSV (Fig. S21), a larger increment of current density with the addition of PMS on *sp*-CoMn@NG compared with that on *p*-CoMn@NG, Mn@NG, Co@NG, and NG. These results collectively suggested that PMS activation was closely dependent on the direct electron transfer and DO contribution, moreover, the axially coordinated Co-Mn bond acted as an “electron bridge” to facilitate electron transfer between LVF and PMS/dissolved oxygen for the degradation of pollutants.

### 3.4. Activation process on axial coordinated sites

The activation of PMS was previously reported to proceed via a non-radical process (i.e.,  $^1\text{O}_2$ ) in *p*-CoMn@NG/PMS system [40]. The  $^1\text{O}_2$  generation path was inclined to react with respect to: PMS<sup>\*</sup>→OH<sup>\*</sup>→O<sup>•</sup>→ $^1\text{O}_2$ . To delve into the catalytic discrepancies and synergies of the axial coordinated Co-Mn (*s*-CoMn@NG) catalysis activities, the overall stimulation steps from PMS to  $^1\text{O}_2$  with the

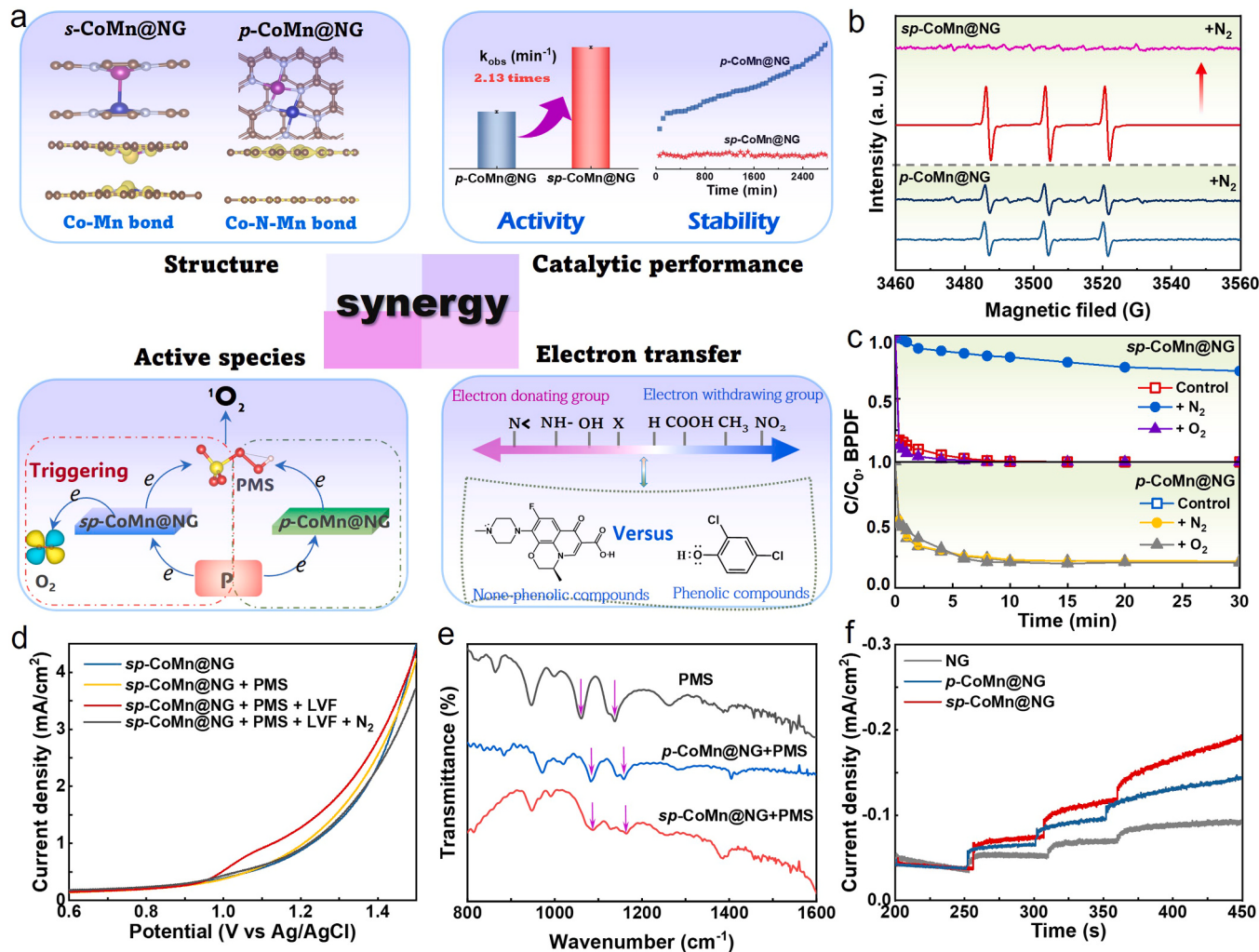
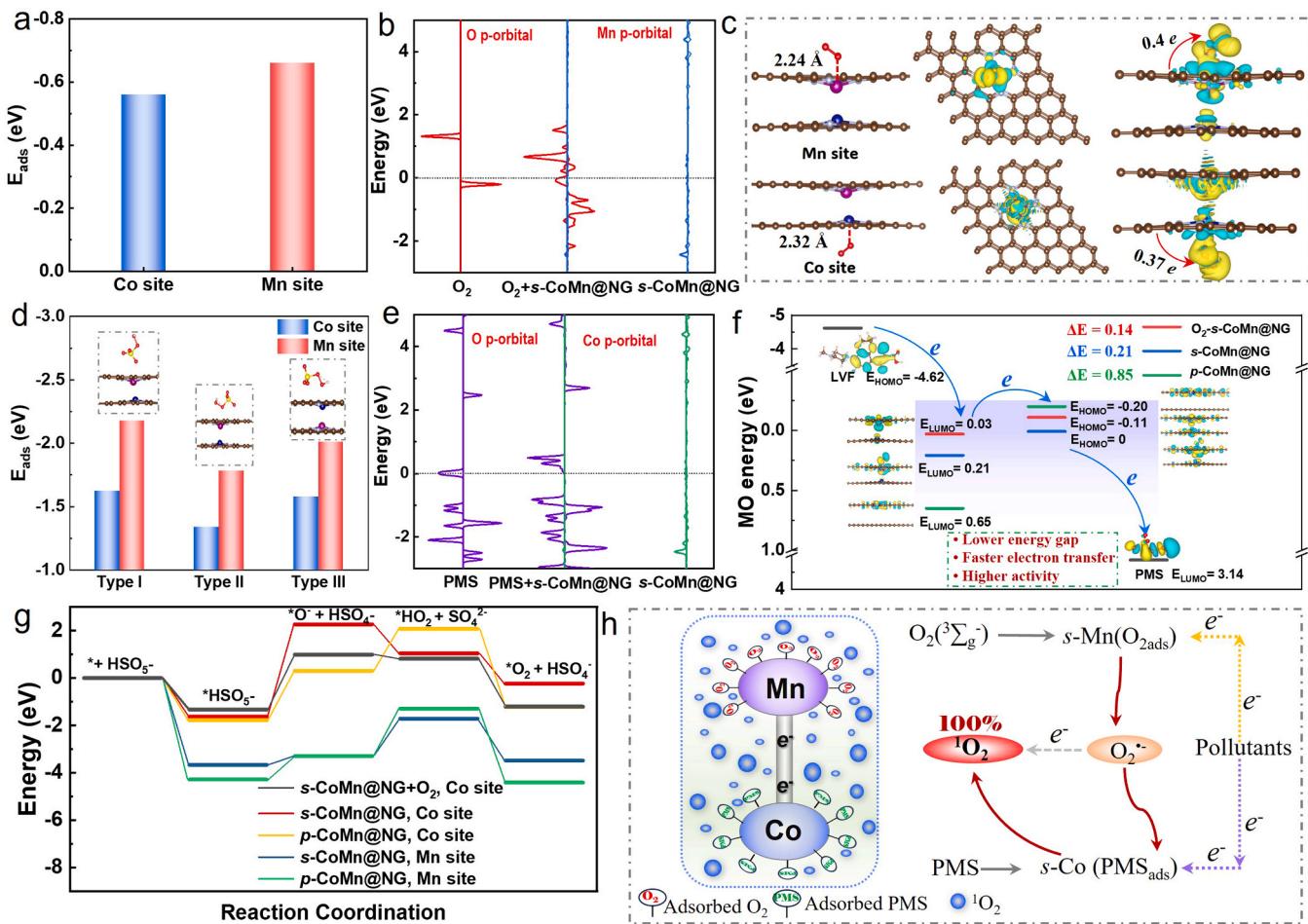


**Fig. 3.** (a) Overview of strategies to compare the differences in *s*-CoMn@NG and *p*-CoMn@NG. EPR spectra (b) and the degradation of DPBF (c) of *sp*-CoMn@NG and *p*-CoMn@NG system with/without  $\text{N}_2$  or  $\text{O}_2$ . (d) Linear sweep voltammetry of samples at different conditions. (e) FTIR spectra of PMS, *p*-CoMn@NG/PMS, and *sp*-CoMn@NG/PMS. (f) Current density of different catalysts with the addition of PMS (1 mL, 1 mM).

contribution of  $\text{O}_2$  were thermodynamically analyzed by DFT (Fig. S22). The projected density of state (PDOS) is shown in Fig. 1c, where an obvious peak of *s*-CoMn@NG is located at the Fermi level, indicating a tight electronic coupling between Mn and Co in *s*-CoMn@NG. Using the adsorption energy of  $\text{O}_2$  as the descriptor, Mn atom shows the larger  $E_{\text{adsO}_2}$  value (-0.66 eV, Fig. 4a and S23) than Co atom (-0.56 eV), suggesting the favorable  $\text{O}_2$  adsorption sites of Mn. The  $\pi^*$  orbital of  $\text{O}_2$  molecule is downshifted below the Fermi level (Fig. 4b), which is due to the *p* orbital of  $\text{O}_2$  interacts with the *p* orbital of Mn atoms to form hybrid states [41]. The charge transfer number of Mn and O (-0.40 e, Fig. 4c) in *s*-CoMn@NG increases after the  $\text{O}_2$  adsorption compared with that of Co and O (-0.37 e), indicating that the electron-grabbing power of  $\text{O}_2$  is enhanced in the axial coordinated microenvironment. The electrostatic potentials mapping was used to reflect the charge distribution of *s*-CoMn@NG before and after  $\text{O}_2$  adsorption (Fig. 4f and S24), the lower energy barrier of  $\text{O}_2+s$ -CoMn@NG (0.14 eV) was observed, implying the enhanced electron migration from the lower unoccupied molecular orbital (LUMO) to the highest occupied molecular orbital (HOMO) after  $\text{O}_2$  introduction. The charge density difference and corresponding adsorption energies ( $E_{\text{ads}}$ ) of PMS showed that the localized electrons and the delocalized charge accumulated along the metal center, implying a strong binding for PMS molecule on both Co and Mn sites (Fig. 4d). Generally, the PMS activation to ROS is a process calling for electron transfer and PMS\* is usually regarded as potential determining

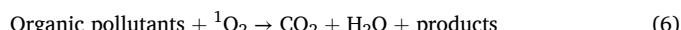
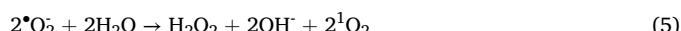
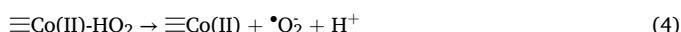
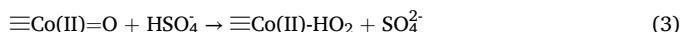
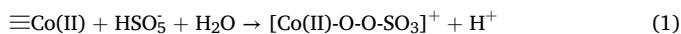
intermediate. Three different kinds of adsorption types of PMS\* formation on Mn/Co sites on *s*-CoMn@NG were presented, in which type I was the more favorable adsorption type for PMS activation. Especially, *p* orbital of PMS interacting with the *p* orbital of Co atoms were also observed, verifying the electron transfer between PMS and Co atom (Fig. 4e). So *s*-CoMn@NG works as the conductive bridge to boost the electron migration from the electron donor (LVF) to the electron acceptor (surface-confined PMS\* complexes) without generating free radicals (Fig. 4f). Benefiting from the narrowest energy gap of *s*-CoMn@NG (0.21 eV), the electrons localized at the HOMO (-4.62 eV) of LVF can be readily transferred to the LUMO (3.14 eV) of metastable PMS\* reactive complex via the metal tunnel driven by a potential energy difference, eventually triggering PMS decomposition.

Fig. 4g illustrated the potential energy surface of PMS dissociation on axial coordinated Co-Mn sites to the possible pathway of  ${}^1\text{O}_2$  formation in *s*-CoMn@NG/PMS system. A PMS molecule would prefer to chemically adsorb on the electron-efficient axial coordinated Co site of *s*-CoMn@NG accompanied by rapid electron accumulation and depletion to form  $\equiv\text{Co}(\text{II})-\text{O}-\text{O}-\text{SO}_3$  complexes with energy change of -1.62 eV. The heterolytic cleavage of the O-O bond in this metastable intermediate ( $\equiv\text{Co}(\text{II})-\text{O}-\text{O}-\text{SO}_3$ ) quickly produced adsorbed oxygen species ( $\equiv\text{Co}(\text{III})=\text{O}$ ) and  $\text{HSO}_4^-$ . Then, the  $\equiv\text{Co}(\text{III})=\text{O}$  further reacted with another PMS molecule in the system to produce active  $\equiv\text{Co}(\text{III})-\text{HO}_2$  species. After the fast deprotonation process of  $\equiv\text{Co}(\text{III})-\text{HO}_2$  species,  $\cdot\text{O}_2^-$



**Fig. 4.** DFT calculation unravels the mechanism of  $O_2$ -triggering PMS activation under the axial coordination microenvironments.  $E_{ads}$  of  $O_2$  on Co and Mn sites (a) of  $s$ -CoMn@NG, and corresponding DOS (b) from the p-orbitals of O and Mn. (c) Charge analysis of Co and Mn sites for  $O_2$  adsorption. (d) Three types of PMS adsorption on Co and Mn sites of  $s$ -CoMn@NG, and corresponding DOS (e) from the p-orbitals of O and Co. (f) The proposed overall PMS activation mechanism on  $s$ -CoMn@NG,  $O_2 + s$ -CoMn@NG, and  $p$ -CoMn@NG. (g) The transient (TS) and free energy for PMS activation on Co and Mn sites of  $s$ -CoMn@NG and  $p$ -CoMn@NG. (h) Schematic of Co and Mn sites for the adsorption of PMS and  $O_2$ , respectively, and the effective electron transfer by the axial bond for  $^1O_2$  production.

radicals were formed along with the breakage of Co-O bond. Eventually,  $^{\bullet}O_2$  radicals recombined to produce plenty of  $^1O_2$  for pollutant degradation [42].



The overall process in Co sites of  $s$ -CoMn@NG+ $O_2$  was thermodynamically more favorable, and a lower total exothermic energy indicated that  $^1O_2$  could be easily generated from the intimate interaction between PMS and Co sites. Notably, the efficient adsorption of  $O_2$  on Mn sites increases the electron-deficient of the axial coordinated Co-Mn sites, facilitating electron transfer and lower energy barrier for  $^1O_2$  generation. In consideration of the obtained results, the possible mechanism for pollutant degradation over axial coordinated Co-Mn sites by PMS activation could be proposed and depicted in Fig. 4h.  $O_2$  is adsorbed on Mn sites, and further activate to form  $O_2^{\bullet}$  intermediates by directly electron transfer from pollutants, which accumulating chiefly around Co-Mn region. PMS can be effectively adsorbed on opposite Co

sites, and then it can be desorbed to form  $^1O_2$  in the role of  $O_2^{\bullet}$  intermediates, accompanying electron transfer through axial Co-Mn bond [43–45]. Combined with the analysis of radical scavenging tests and EPR experiments, the pathways of  $^1O_2$  production by the self-desorption of PMS and recombination of  $O_2^{\bullet}$  can be negligible. Thus, the axially coordinated Co-Mn active center of  $sp$ -CoMn@NG offers additional mechanistic insights into the favorable  $^1O_2$  generation.

### 3.5. Potential environmental applications

$sp$ -CoTH@NG exhibited commendable efficiency in degrading LVF in natural waters (tap water, lake water, river water, and DI water, Fig. 5a and S25). Notably, a discernible disparity in degradation rate constants was observed, with DI water demonstrating a notably higher rate. This discrepancy can be attributed to the elevated levels of dissolved oxygen in DI water in comparison to other natural water bodies. Such findings underscore the pivotal contribution of  $^1O_2$  originating from dissolved oxygen within the  $sp$ -CoMn@NG/PMS system. Nevertheless, it is imperative to acknowledge the presence of coexisting environmental ions in tap, lake and river water, which induced synthetic effects leading to a slight decrease in degradation rate constants (Fig. S13). Various kinds of pollutants were tested in this system (Fig. S26), including LVF, methylene blue (MB), ciprofloxacin (CIP), 4-chlorophenol (4-CP), bisphenol A (BPA), nitrobenzene (NB), and 2,4-dichlorophenol (2,4-DCP). Correspondingly, the  $k_{obs}$  of these organic compounds by the  $sp$ -

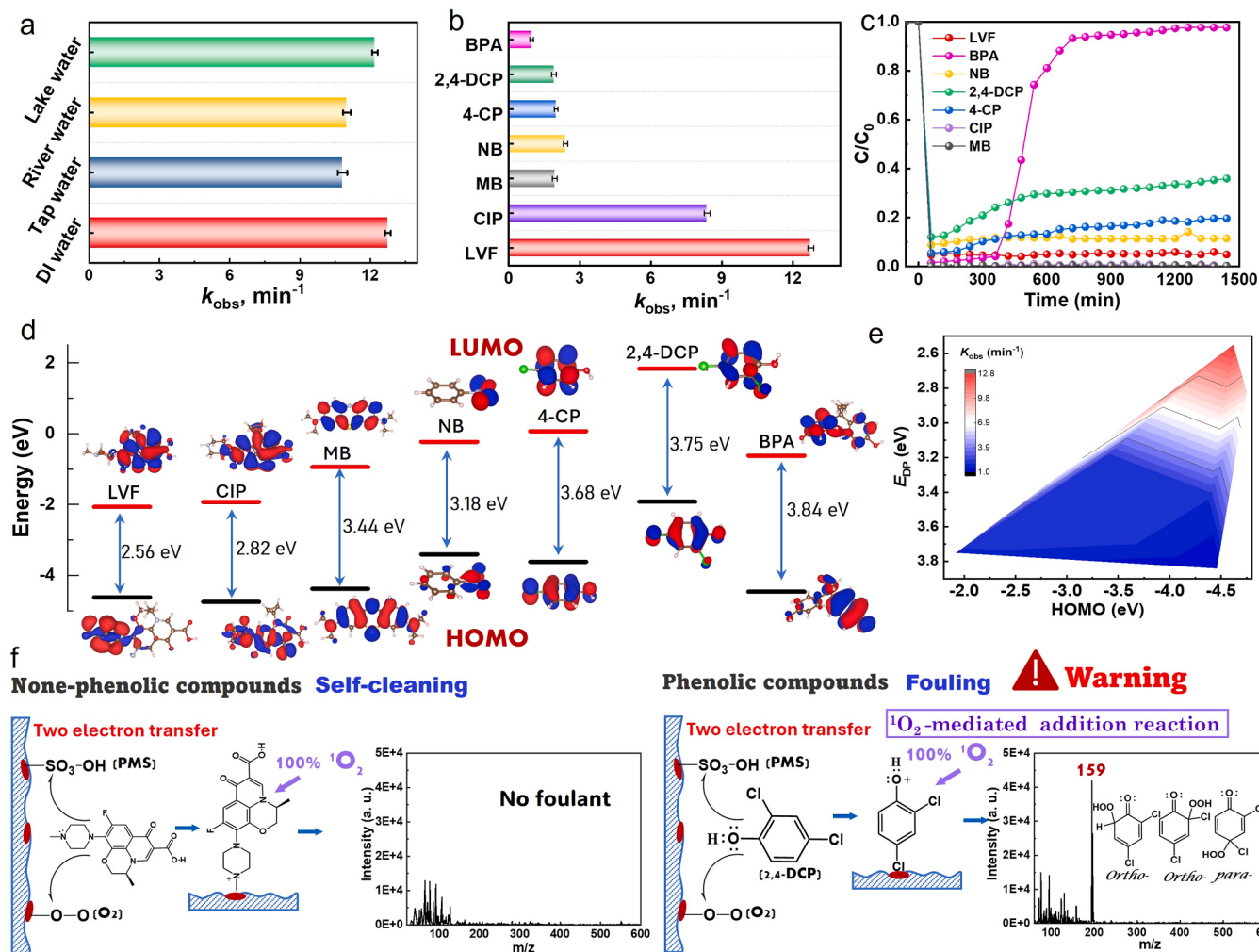


**Fig. 5.** (a) Degradation rate constants of LVF in different natural waters. (b) Rate constants in batching system of *sp*-CoMn@NG for different refractory pollutants (LVF, BPA, NB, MB, CIP, 4-CP, and 2,4-DCP). [LVF/BPA/NB/MB/CIP/4-CP/2,4-DCP] = 25 ± 1 mg L<sup>-1</sup>, [PMS] = 1.0 ± 0.1 mM, pH = 5.8, T = 25 °C. (c) The removal performance of different pollutants in the flowing-through system. (d) HOMO and LUMO of various organic molecules. (e) Correlation between  $k_{\text{obs}}$  and HOMO levels/ $E_{\text{PD}}$ . (f) Schematic  $^1\text{O}_2$ -mediated reaction pathway for the non-phenolic and phenolic compounds, liquid chromatogram and mass spectrum of products washed off by ethanol of LVF and 2,4-DCP, and the energies are shown in kJ/mol and relative to 2,4-DCP +  $^1\text{O}_2$  reaction at the DFT/B3LYP/6–311 G level of theory.

CoMn@NG/PMS system increased in the following order (Fig. 5b): BPA (0.97 min<sup>-1</sup>) < 2,4-DCP (1.91 min<sup>-1</sup>) < MB (1.94 min<sup>-1</sup>) < 4-CP (2.00 min<sup>-1</sup>) < NB (2.40 min<sup>-1</sup>) < CIP (8.37 min<sup>-1</sup>) < LVF (12.75 min<sup>-1</sup>). Remarkably, the  $k_{\text{obs}}$  of BPA also outperforms most catalysts in reported works (Fig. S27 and Table S5). Moreover, we observed that the adsorption capacities of these pollutants (BPA < 2,4-DCP < 4-CP < CIP < LVF, Fig. S28) were positively correlated with  $k_{\text{obs}}$ . However, excessively high adsorption capacities (NB and MB) resulted in a decreased in  $k_{\text{obs}}$ . The turnover frequencies (TOFs) of Co-Mn sites on *sp*-CoMn@NG exhibited the superior reaction activity, which is higher than other ASCs (Fig. S29-S30 and Table S6). Moreover, *sp*-CoMn@NG were filtered to be a membrane for *in-situ* PMS activation to degrade refractory pollutant in a flow-through system (Fig. S31). Results showed that the non-phenolic compounds (LVF, CIP, MB, and NB) can be effectively and stably degraded in long-time running (>1500 min, Fig. 5c). Whereas the removal performance of BPA quickly decreased from 99.8% to 4.0%, as well as other phenolic compounds (2,4-DCP and 4-CP) decreased continuously in long-time running.

Delocalized  $\pi$  electrons from lone-pair electrons from functional groups on pollutants can be delivered for  $^1\text{O}_2$  production, in which direct electron transfer from pollutants to generate  $^1\text{O}_2$  instead of  $\text{SO}_4^{2-}$ . To validate this potential energy difference-driven electron transfer, the selected compounds with different molecular structures exhibited

distinct disparity in the HOMO-LUMO energy levels as well as potential differences ( $E_{\text{PD}}$ ) (Fig. 5d). As is known, more negative HOMO value display a stronger electron donating ability, and narrow  $E_{\text{PD}}$  facilitates to electron transfer [46]. The  $k_{\text{obs}}$  constants in PMS-mediated catalysts have a close relationship with HOMO level and  $E_{\text{PD}}$  of organic compounds (Fig. 5e). An organic pollutant with a large negative HOMO value and small  $E_{\text{PD}}$  value could be more easily degraded by donating more electrons for improving catalytic reaction. Results not only consolidate the proposed mechanism of potential energy difference-drive electron transfer but also clarify the origin of catalytic activity of heteroatoms doping.

As aforementioned, the stability of *sp*-CoMn@NG membrane is closely related to the structures of pollutants, and the removal efficiencies of some phenolic compounds (2,4-DCP, 4-CP, and BPA) continuously decreased in long-term running, attributing to active sites poisoning. The recognized applications of  $^1\text{O}_2$  reactions are domino and tandem process, and phenolic hydroxyl groups are the favorable sites for potential reaction [47]. Fig. S32 showed TOC removal performance on *sp*-CoMn@NG in following order: LVF (90.1%) > CIP (77.1%) > NB (54.8%) > MB (43.8%) > 4-CP (10.1%) ≈ 2,4-DCP (10.0%) > BPA (0.2%), indicating the low mineralization degree of phenolic compounds. These results were positively correlative with the stability of removal performance, thus we proposed that  $^1\text{O}_2$ -mediated catalysis can

degrade phenolic compounds by addition reaction to form hydroperoxide products, leading to the active site poisoning.

To explore the mechanism of active site poisoning, we used liquid chromatography-mass spectrometry (LC-MS) to analyze the dissolved products of LVF (as a representative non-phenolic compound) and 2,4-DCP (as a representative phenolic compound). As predicted, there is no product can be detected after treating LVF (Fig. 5f), indicating that no foulant deposited on *sp*-CoMn@NG surface and pollutants can be efficiently degraded into small molecules. Whereas some foulants were formed on *sp*-CoMn@NG surface after treating 2,4-DCP, and these foulants were identified as the addition compounds (*m/z* = 194, Fig. S33, allyl hydroperoxide and hydroperoxide ketones) generated by the addition reaction of 2,4-DCP and  $^1\text{O}_2$  on its *ortho*- and *para*- position of the phenolic-hydroxyl group and then they can be further coupled and polymerized [48]. These products were more toxicity than 2,4-DCP by the analysis of fathead minnow LC50, bioaccumulation factor, developmental toxicity, and mutagenicity (Fig. S34) [49]. Specifically, the Gibbs energies of  $-124.97\text{ kJ/mol}$  of pathway 1 (P1),  $-134.16\text{ kJ/mol}$  of pathway 2 (P2), and  $-148.08\text{ kJ/mol}$  of pathway 3 (P3), respectively, further verified the feasibility of addition reaction of  $^1\text{O}_2$  and 2,4-DCP. Similarly, some compounds were also generated after treating BPA (Fig. S35-36) and the corresponding Gibbs energies were  $-116.83\text{ kJ/mol}$  and  $-237.87\text{ kJ/mol}$ .

Overall,  $^1\text{O}_2$  can undergo addition reactions with phenolic-hydroxyl compounds at the double bond of the phenolic ring, forming various addition products such as hydroperoxides, epoxides, or other oxygenated species. These products can accumulate on the active sites of catalytic membranes, causing blockage or hinderance. Over time, this accumulation renders the catalytic membrane ineffective in removing pollutants, leading to decreased efficiency, compromised water quality, and potential increases in operational costs due to the need for membrane replacement or regeneration. Consequently, the direct reaction of  $^1\text{O}_2$  with phenolic-hydroxyl compounds can generate addition products that deactivate the active sites of catalytic membranes, ultimately rendering them ineffective. Understanding and addressing this process is essential for the development and maintenance of efficient water treatment systems.

#### 4. Conclusion

In summary, we have developed the dual-atom Co-Mn site with axial and planar coordination on N-doped graphene catalyst, which realizes nearly 100% PMS conversion to  $^1\text{O}_2$  through dissolved oxygen triggering in a flow-through membrane system. This automated, sustainable and scalable approach of highly efficient  $^1\text{O}_2$  production and utilization has promising potential in diverse applications, including targeted water purification and *in-situ* sensing in environmental remediation, green organic synthesis, and biomedical engineering. *sp*-CoMn@NG achieves the effective *in-situ* degradation of organic pollutants with high turnover frequency, exhibiting approximately 159.4 times of rate constant for levofloxacin degradation higher than N-doped graphene. Experiments and DFT simulations confirm that PMS and  $\text{O}_2$  are adsorbed on Co and Mn site, respectively, which can be activated to form  $\text{O}_2^\bullet$  intermediate by direct electron transfer, and then the adsorbed PMS can be desorbed from  $^1\text{O}_2$  by  $\text{O}_2^\bullet$ . Of note, addition reaction can occur on the phenolic compounds, where  $^1\text{O}_2$  can be directly additive onto phenolic hydroxyl groups to form some hydroperoxide compounds, leading to the active sites poisoning and the invalidation of catalytic membrane. This work opens up a new avenue for the scalable and automated  $^1\text{O}_2$  production in an innovation reactive membrane filtration, and also unveils the practical potential of  $^1\text{O}_2$ -mediated degradation of phenolic organic compounds.

#### CRediT authorship contribution statement

**Minghua Zhou:** Writing – review & editing, Supervision, Resources,

Project administration. **Meilan Pan:** Writing – review & editing, Supervision, Project administration, Conceptualization. **Cong Li:** Methodology, Data curation. **Lingling Xu:** Methodology, Investigation, Data curation. **Hanwen Gong:** Writing – original draft, Methodology, Investigation, Data curation.

#### Declaration of Competing Interest

The authors declare that they have no known competing financial interests or personal relationships that could have appeared to influence the work reported in this paper.

#### Data Availability

Data will be made available on request.

#### Acknowledgements

We gratefully acknowledge the financial support from the National Natural Science Foundation of China (Grant No. 22106139 and 52170085), and Basic Scientific Research Projects in Colleges and Universities funded by Zhejiang Province (RF-A2022009).

#### Appendix A. Supporting information

Supplementary data associated with this article can be found in the online version at doi:10.1016/j.apcatb.2024.124202.

#### References

- [1] M. Huang, Y. Han, W. Xiang, D. Zhong, C. Wang, T. Zhou, X. Wu, J. Mao, In situ-formed phenoxyl radical on the CuO surface triggers efficient persulfate activation for phenol degradation, Environ. Sci. Technol. 55 (2021) 15361–15370.
- [2] X. Duan, H. Sun, J. Kang, Y. Wang, S. Indrawirawan, S. Wang, Insights into heterogeneous catalysis of persulfate activation on dimensional-structured nanocarbons, ACS Catal. 5 (2015) 4629–4636.
- [3] S. Cai, Q. Zhang, Z. Wang, S. Hua, D. Ding, T. Cai, R. Zhang, Pyrolytic N-rich biochar without exogenous nitrogen doping as a functional material for bisphenol A removal: performance and mechanism, Appl. Catal. B-Environ. 291 (2021) 120093.
- [4] Y. Chen, G. Zhang, H. Liu, J. Qu, Confining free radicals in close vicinity to contaminants enables ultrafast Fenton-like processes in the interspacing of Mo<sub>2</sub> membranes, Angew. Chem. Int. Ed. 58 (2019) 8134–8138.
- [5] X. Zhang, S. Liu, Z. Wang, K. Feng, S. Xu, X. Li, P. Yu, X. Fan, H. Zheng, Y. Sun, Inert magnesium-doped Co<sub>3</sub>O<sub>4</sub> spinel assembling catalytic membrane for instantaneous peroxymonosulfate activation and contaminants elimination, Chem. Eng. J. 477 (2023) 146987.
- [6] L.S. Zhang, X.H. Jiang, Z.A. Zhong, L. Tian, Q. Sun, Y.T. Cui, X. Lu, J.P. Zou, S. L. Luo, Carbon nitride supported high-loading Fe single-atom catalyst for activation of peroxymonosulfate to generate  $^1\text{O}_2$  with 100% selectivity, Angew. Chem. Int. Ed. 60 (2021) 21751–21755.
- [7] Y. Bu, H. Li, W. Yu, Y. Pan, L. Li, Y. Wang, L. Pu, J. Ding, G. Gao, B. Pan, Peroxydisulfate activation and singlet oxygen generation by oxygen vacancy for degradation of contaminants, Environ. Sci. Technol. 55 (2021) 2110–2120.
- [8] N. Zhao, K. Liu, C. He, J. Gao, W. Zhang, T. Zhao, D.C.W. Tsang, R. Qiu, Singlet oxygen mediated the selective removal of oxytetracycline in C/Fe<sub>3</sub>C/Fe<sup>0</sup> system as compared to chloramphenicol, Environ. Int. 143 (2020) 105899.
- [9] T. Li, L. Ge, X. Peng, W. Wang, W. Zhang, Enhanced degradation of sulfamethoxazole by a novel Fenton-like system with significantly reduced consumption of H<sub>2</sub>O<sub>2</sub> activated by g-C<sub>3</sub>N<sub>4</sub>/MgO composite, Water Res 190 (2021) 116777.
- [10] N. Du, Y. Liu, Q. Li, W. Miao, D. Wang, S. Mao, Peroxydisulfate activation by atomically-dispersed Fe-Nx on N-doped carbon: Mechanism of singlet oxygen evolution for nonradical degradation of aqueous contaminants, Chem. Eng. J. 413 (2021) 127545.
- [11] T. Ouyang, A.-N. Chen, Z.-Z. He, Z.-Q. Liu, Y. Tong, Rational design of atomically dispersed nickel active sites in  $\beta$ -Mo<sub>2</sub>C for the hydrogen evolution reaction at all pH values, Chem. Commun. 54 (2018) 9901–9904.
- [12] H. Qi, J. Yang, F. Liu, L. Zhang, J. Yang, X. Liu, L. Li, Y. Su, Y. Liu, R. Hao, A. Wang, T. Zhang, Highly selective and robust single-atom catalyst Ru1/NC for reductive amination of aldehydes/ketones, Nat. Commun. 12 (2021) 3295.
- [13] C. Xia, Y. Qiu, Y. Xia, P. Zhu, G. King, X. Zhang, Z. Wu, J.Y. Kim, D.A. Cullen, D. Zheng, P. Li, M. Shakouri, E. Heredia, P. Cui, H.N. Alshareef, Y. Hu, H. Wang, General synthesis of single-atom catalysts with high metal loading using graphene quantum dots, Nat. Chem. 13 (2021) 887–894.
- [14] S. Zuo, X. Jin, X. Wang, Y. Lu, Q. Zhu, J. Wang, W. Liu, Y. Du, J. Wang, Sandwich structure stabilized atomic Fe catalyst for highly efficient Fenton-like reaction at all pH values, Appl. Catal. B-Environ. 282 (2021) 119551.

[15] X. Mi, P. Wang, S. Xu, L. Su, H. Zhong, H. Wang, Y. Li, S. Zhan, Almost 100% peroxymonosulfate conversion to singlet oxygen on single-atom  $\text{CoN}_{2+2}$  sites, *Angew. Chem. Int. Ed. Engl.* 60 (2021) 4588–4593.

[16] X. Liu, Y. Liu, W. Yang, X. Feng, B. Wang, Controlled modification of axial coordination for transition-metal single-atom electrocatalyst, *Chem. Eur. J.* 28 (2022) 202201471.

[17] Z. Zeng, L.Y. Gan, H. Bin Yang, X. Su, J. Gao, W. Liu, H. Matsumoto, J. Gong, J. Zhang, W. Cai, Z. Zhang, Y. Yan, B. Liu, P. Chen, Orbital coupling of heteroditomatic nickel-iron site for bifunctional electrocatalysis of  $\text{CO}_2$  reduction and oxygen evolution, *Nat. Commun.* 12 (2021) 4088.

[18] L. Zhang, N. Jin, Y. Yang, X.-Y. Miao, H. Wang, J. Luo, L. Han, Advances on axial coordination design of aingle-atom catalysts for energy electrocatalysis: a review, *Nano-Micro Lett.* 15 (2023) 228.

[19] W.S.Yi Li, M.J. Zachman, M. Wang, S. Hwang, H. Tabassum, J. Yang, X. Yang, S. Karakalos, Z. Feng, G. Wang, G. Wu, Atomically dispersed dual-metal site catalysts for enhanced  $\text{CO}_2$  reduction: mechanistic insight into active site structures, *Angew. Chem. Int. Ed. Engl.* 61 (2022) 202205632.

[20] Y. Liu, Y. Su, J. Guan, J. Cao, R. Zhang, M. He, K. Gao, L. Zhou, Z. Jiang, 2D heterostructure membranes with sunlight-driven self-cleaning ability for highly efficient oil-water separation, *Adv. Funct. Mater.* 28 (2018) 1706545.

[21] Y.J. Zhang, G.X. Huang, L.R. Winter, J.J. Chen, L. Tian, S.C. Mei, Z. Zhang, F. Chen, Z.Y. Guo, R. Ji, Y.Z. You, W.W. Li, X.W. Liu, H.Q. Yu, M. Elimelech, Simultaneous nanocatalytic surface activation of pollutants and oxidants for highly efficient water decontamination, *Nat. Commun.* 13 (2022) 3005.

[22] A.G. Griesbeck, A. deKiff, M. Kleczka, Tetraphenylporphyrin-catalyzed tandem photooxygenation of polyenes and 1,4-dienes: multiple and diverse oxyfunctionalizations, *Adv. Syn. Catal.* 356 (2014) 2839–2845.

[23] A.G. Griesbeck, V. Schlundt, J.M. Neudörfl, Functionalized polar 1,2,4-trioxanes as building blocks by singlet oxygenation of 4-hydroxy tiglic acid using the solvent deuterium isotope trick, *Org. Lett.* 3 (2013) 7265.

[24] Maria Tofi, Konstantina Koltsida, G. Vassilikogiannakis, Singlet-oxygen-mediated one-pot synthesis of 3-keto-tetrahydrofurans from 2-( $\beta$ -hydroxyalkyl) furans, *Org. Lett.* 11 (2009) 313–316.

[25] N. Jiang, H. Xu, L. Wang, J. Jiang, T. Zhang, Nonradical oxidation of pollutants with single-atom-Fe(III)-activated persulfate: Fe(V) being the possible intermediate oxidant, *Environ. Sci. Technol.* 54 (2020) 14057–14065.

[26] L. Liu, Q. Liu, Y. Wang, J. Huang, W. Wang, L. Duan, X. Yang, X. Yu, X. Han, N. Liu, Nonradical activation of peroxydisulfate promoted by oxygen vacancy-laden  $\text{NiO}$  for catalytic phenol oxidative polymerization, *Appl. Catal. B-Environ.* 254 (2019) 166–173.

[27] Y. Wang, Y. Wu, Y. Yu, T. Pan, D. Li, D. Lambropoulou, X. Yang, Natural polyphenols enhanced the Cu(II)/peroxymonosulfate (PMS) oxidation: the contribution of Cu(III) and HO, *Water Res.* 186 (2020) 116326.

[28] J. Gao, Y. Feng, W. Guo, L. Jiang, Nanofluidics in two-dimensional layered materials: inspirations from nature, *Chem. Soc. Rev.* 46 (2017) 5400–5424.

[29] A.K. Geim, K.S. Novoselov, The rise of graphene, *Nat. Mater.* 6 (2007) 183–191.

[30] M. Pan, S. Liu, J.W. Chew, Realizing the intrinsic electrochemical activity of acidic N-doped graphene through 1-pyrenesulfonic acid bridges, *Adv. Funct. Mater.* (2020) 2001237.

[31] Y. Sun, X. Li, T. Zhang, K. Xu, Y. Yang, G. Chen, C. Li, Y. Xie, Nitrogen-doped cobalt diselenide with cubic phase maintained for enhanced alkaline hydrogen evolution, *Angew. Chem. Int. Ed. Engl.* 60 (2021) 21575–21582.

[32] M. Pan, J. Wang, G. Gao, J.W. Chew, Incorporation of single cobalt active sites onto N-doped graphene for superior conductive membranes in electrochemical filtration, *J. Membr. Sci.* 602 (2020) 117966.

[33] Z. Li, S. Gadipelli, H. Li, C.A. Howard, D.J.L. Brett, P.R. Shearing, Z. Guo, I. P. Parkin, F. Li, Tuning the interlayer spacing of graphene laminate films for efficient pore utilization towards compact capacitive energy storage, *Nat. Energy* 5 (2020) 160–168.

[34] M. Pan, J. Li, X. Zhang, S. Liu, J.W. Chew, B. Pan, Axially coordinated  $\text{Co-N}_4$  sites for the electroreduction of nitrobenzene, *J. Mater. Chem. A* (2023) 5095–5103.

[35] Y. Peng, B. Lu, S. Chen, Carbon-supported single atom catalysts for electrochemical energy conversion and storage, *Adv. Mater.* 30 (2018) 1801995.

[36] J. Wang, X. Huang, S. Xi, H. Xu, X. Wang, Axial modification of cobalt complexes on heterogeneous surface with enhanced electron transfer for carbon dioxide reduction, *Angew. Chem. Int. Ed. Engl.* 59 (2020) 19162–19167.

[37] G.S. Timmins, K.J. Liu, E.J.H. Bechara, Y. Kotake, H.M. Swartz, Trapping of free radicals with direct in vivo EPR detection: a comparison of 5,5-dimethyl-1-pyrroline-N-oxide and 5-diethoxyphosphoryl-5-methyl-1-pyrroline-N-oxide as spin traps for  $\text{HO}\cdot$  and  $\text{SO}_4\cdot$ , *Free Radic. Bio. Med.* 27 (1999) 329–333.

[38] J.H. Wu, F. Chen, T.H. Yang, H.Q. Yu, Unveiling singlet oxygen spin trapping in catalytic oxidation processes using in situ kinetic EPR analysis, *Proc. Natl. Acad. Sci. USA* 120 (2023), 2305706120.

[39] Z. Weng, Y. Lin, S. Guo, X. Zhang, Q. Guo, Y. Luo, X. Ou, J. Ma, Y. Zhou, J. Jiang, B. Han, Site engineering of covalent organic frameworks for regulating peroxymonosulfate activation to generate singlet oxygen with 100% selectivity, *Angew. Chem. Int. Ed. Engl.* (2023), <https://doi.org/10.1002/anie.202310934>.

[40] Y. Yao, C. Wang, Y. Yang, S. Zhang, X. Yan, C. Xiao, Y. Zhou, Z. Zhu, J. Qi, X. Sun, J. Li, Mn-Co dual sites relay activation of peroxymonosulfate for accelerated decontamination, *Appl. Catal. B-Environ.* 330 (2023) 122656.

[41] T. Wang, X. Cao, H. Qin, L. Shang, S. Zheng, F. Fang, L. Jiao, P-block qtomically dispersed antimony catalyst for highly efficient oxygen reduction reaction, *Angew. Chem. Int. Ed. Engl.* 60 (2021) 21237–21241.

[42] J. He, Y. Wan, W. Zhou, ZIF-8 derived Fe-N coordination moieties anchored carbon nanocubes for efficient peroxymonosulfate activation via non-radical pathways: role of FeNx sites, *J. Hazard. Mater.* 405 (2021) 124199.

[43] J. Wang, B. Li, Y. Li, X. Fan, F. Zhang, G. Zhang, Y. Zhu, W. Peng, Easily regenerated  $\text{CuO}/\text{gamma-Al}_2\text{O}_3$  for persulfate-based catalytic oxidation: insights into the deactivation and regeneration mechanism, *ACS Appl. Mater. Interfaces* 13 (2021) 2630–2641.

[44] Z. Yang, J. Qian, A. Yu, B. Pan, Singlet oxygen mediated iron-based Fenton-like catalysis under nanoconfinement, *Proc. Natl. Acad. Sci. USA* 116 (2019) 6659–6664.

[45] L. Liu, Y. Wang, Q. Liu, W. Wang, L. Duan, X. Yang, S. Yi, X. Xue, J. Zhang, Activating peroxydisulfate by morphology-dependent  $\text{NiO}$  catalysts: structural origin of different catalytic properties, *Appl. Catal. B-Environ.* 256 (2019) 117806.

[46] J. Dou, J. Cheng, Z. Lu, Z. Tian, J. Xu, Y. He, Biochar co-doped with nitrogen and boron switching the free radical based peroxydisulfate activation into the electron-transfer dominated nonradical process, *Appl. Catal. B-Environ.* 301 (2022) 120832.

[47] A.A. Ghogare, A. Greer, Using singlet oxygen to synthesize natural products and drugs, *Chem. Rev.* 116 (2016) 9994–10034.

[48] Q. Song, T. Niu, H. Wang, Theoretical study of the reaction of 2,4-dichlorophenol with  $^1\text{O}_2$ , *J. Mol. Struct.* 861 (2008) 27–32.

[49] M. Pan, C. Li, X. Wei, G. Liu, E.H. Ang, B. Pan, Pioneering piezoelectric-driven atomic hydrogen for efficient dehalogenation of halogenated organic pollutants, *Environ. Sci. Technol.* 58 (2024) 4008–4018.